Siyi Liu
Department of Aerospace Engineering
and Engineering Mechanics,
Center for Mechanics of Solids,
Structures and Materials,
The University of Texas at Austin,
Austin, TX 78712
e-mail: liusiyi@utexas.edu

Taewoo Ha
Department of Electrical and Computer
Engineering,
The University of Texas at Austin,
Austin, TX 78712
e-mail: th25236@utexas.edu

Nanshu Lu[1]
Mem. ASME
Department of Aerospace Engineering
and Engineering Mechanics,
Center for Mechanics of Solids,
Structures and Materials,
The University of Texas at Austin,
210 E. 24th Street,
Austin, TX 78712;
Department of Electrical and Computer
Engineering,
The University of Texas at Austin,
Austin, TX 78712;
Department of Biomedical Engineering,
The University of Texas at Austin,
Austin, TX 78712;
Texas Materials Institute,
The University of Texas at Austin,
Austin, TX 78712
e-mail: nanshulu@utexas.edu

Experimentally and Numerically Validated Analytical Solutions to Nonbuckling Piezoelectric Serpentine Ribbons

Emerging stretchable piezoelectric devices have added exciting sensing and energy harvesting capabilities to wearable and implantable soft electronics. As conventional piezoelectric materials are intrinsically stiff and some are even brittle, out-of-plane wrinkled or buckled structures and in-plane serpentine ribbons have been introduced to enhance their compliance and stretchability. Among those stretchable structures, in-plane piezoelectric serpentine ribbons (PSRs) are preferred on account of their manufacturability and low profiles. To elucidate the trade-off between compliance and sensitivity of PSRs of various shapes, we herein report a theoretical framework by combining the piezoelectric plate theory with our previously developed elasticity solutions for passive serpentine ribbons without piezoelectric property. The electric displacement field and the output voltage of a freestanding but nonbuckling PSR under uniaxial stretch can be analytically solved under linear assumptions. Our analytical solutions were validated by finite element modeling (FEM) and experiments using polyvinylidene fluoride (PVDF)-based PSR. In addition to freestanding PSRs, PSRs sandwiched by polymer layers were also investigated by FEM and experiments. We found that thicker and stiffer polymers reduce the stretchability but enhance the voltage output of PSRs. When the matrix is much softer than the piezoelectric material, our analytical solutions to a freestanding PSR are also applicable to the sandwiched ones.
[DOI: 10.1115/1.4042570]

Keywords: stretchable, piezoelectric, serpentine, PVDF, voltage output

1 Introduction

In the past decade, flexible and stretchable electronics have found many exciting applications in bio-integrated electronics [1–3], biomimetic devices [4–6], as well as deployable and conformable devices [7–9]. In addition to conductive and semiconducting materials, there are growing interests in integrating piezoelectric materials in soft bio-electronics for their mechanical sensing, actuation, and energy harvesting capabilities. However, conventional piezoelectric materials, such as lead zirconate titanate (PZT) [10], zinc oxide (ZnO) [11], and polyvinylidene fluoride (PVDF) [12], are much stiffer than soft bio-tissues, which limits their biointegration. To enable the stretchability of piezoelectric devices, researchers borrowed the island-bridge structure [13,14] from stretchable electronics. It consists of isolated stiff functional islands interconnected by electrically conductive in-plane serpentine or buckled ribbons all supported by a stretchable substrate [15–17]. For example, a tissue-conformable stiffness sensor based on PZT islands and serpentine metal interconnects has been reported to survive up to 30% uniaxial tensile strain [18]. Similar stretchability has been achieved for PVDF islands on a thin polydimethylsiloxane substrate [19]. Although these devices are stretchable, separate patterning steps for piezoelectric materials and metal interconnects are required during device fabrication.

As a result, people thought of configuring the piezoelectric materials into a continuous structure that is stretchable. With this concept, many out-of-plane structures, such as the buckled structure [20–22], the woven structure [23,24], and the helical structure [25], have been constructed for piezoelectric devices. However, these out-of-plane structures increase device thickness and also impede their encapsulation and integration with foreign surfaces.

In fact, continuous stretchable structures can be achieved through in-plane designs such as the serpentine ribbons [26–31] and the kirigami cuts made to a planar sheet [32–34]. Compared with the kirigami design, which has to buckle out-of-plane when stretched and consists of many sharp cracks, the serpentine ribbons can deform completely in-plane [7], can be very compliant to stretch [31], and are robust enough to survive overstretch and many deformation cycles [35]. In fact, printed serpentine-shaped PVDF nanofibers/microfibers have been reported with stretchability up to 300% [36,37]. Our group has applied the "cut-and-paste" manufacture to pattern a thin sheet of PVDF into a filamentary serpentine network that can serve as skin-soft and skin-conformable seismocardiogram sensors to measure the chest deformation of a few micron strains [38]. So far, the design of piezoelectric serpentine ribbons (PSRs) is mostly empirical because there is no available theoretical framework for them. Therefore, we want to provide the first set of theoretical analysis on PSRs.

The mechanics of passive serpentines has been well studied in recent years. At small deformation, full-field analytical solutions

[1]Corresponding author.

Contributed by the Applied Mechanics Division of ASME for publication in the Journal of Applied Mechanics. Manuscript received November 16, 2018; final manuscript received January 4, 2019; published online March 16, 2019. Assoc. Editor: Yonggang Huang.

under curved beam [31] and linear elasticity [39] assumptions have been derived for nonbuckling serpentines. However, the linear models significantly overestimate the stretchability when the applied strains are beyond 50%, so finite deformation models were also established for nonbuckling serpentines [40]. Moreover, the buckling and postbuckling behaviors of freestanding serpentines [41–43], polymer-bonded serpentines [44–46], and serpentines exploring self-similar designs [47,48] were also investigated.

Herein, we present a theoretical framework for freestanding nonbuckling PSRs by combining the existing linear elasticity serpentine model [39] with the piezoelectric plate theory [49]. We will validate our analytical results through 3D finite element modeling (FEM) and experiments. We will also examine the effects of a polymer matrix for PSRs embedded in a polymer matrix.

This paper is organized as follows: In Sec. 2, the theoretical framework, the FEM method, and the experimental setup for measuring freestanding PVDF PSRs are described. In Sec. 3, the theoretical, FEM, and experimental results are plotted together for comparison. Section 4 experimentally and numerically investigates PSRs embedded in a polymer matrix and discusses the applicability of our analytical solutions. Concluding remarks are given in Sec. 5.

2 Methods

2.1 Analytical Model. We consider uniaxial tension applied to a periodic PSR. A three-dimensional (3D) schematic of a unit cell of the PSR is depicted in Fig. 1(*a*), where gray represents the piezoelectric material and cyan represents its top and bottom electrodes. In many cases, the surface electrodes are so thin (e.g., 200 nm) compared with the piezoelectric material (e.g., 28 μm) that the mechanical stiffness of the electrodes is negligible. The sidewalls of the PSR are traction-free, charge-free surfaces. The Cartesian coordinate system $\{x, y, z\}$ is used as the global coordinate. The PSR is poled in the z direction and stretched along the x direction. Each unit cell is constructed by linear arms and circular arcs. Its geometry can be fully defined by five independent parameters: the ribbon thickness t, the ribbon width w, the arm length l, the arc radius R, and the arc angle α. Assuming that the serpentine cannot buckle, i.e., can only deform in-plane, it can be modeled as plane stress. In this case, only three independent dimensionless geometric parameters are left: w/R, l/R, and α. With each end being pulled by u_0 for this unit cell, the applied strain is defined by

$$e_{\text{app}} = \frac{2u_0}{L} \tag{1}$$

where L is the linear distance between the two ends of the undeformed unit cell, which can be expressed as

$$L = 4\left(R\cos\alpha - \frac{l}{2}\sin\alpha\right) \tag{2}$$

The PSR is assumed to have isotropic mechanical properties and orthotropic electromechanical properties. Young's modulus Y and Poisson's ratio ν are used to describe the mechanical properties. The electromechanical properties can be described by a 3×6 matrix for the piezoelectric coefficients $\boldsymbol{d}$ following the Voigt notation and a 3×3 matrix for the dielectric constants $\boldsymbol{\varepsilon}$:

$$[d_{ij}] = \begin{bmatrix} 0 & 0 & 0 & 0 & d_{15} & 0 \\ 0 & 0 & 0 & d_{24} & 0 & 0 \\ d_{31} & d_{32} & d_{33} & 0 & 0 & 0 \end{bmatrix}$$
$$[\varepsilon_{ij}] = \begin{bmatrix} \varepsilon_1 & 0 & 0 \\ 0 & \varepsilon_2 & 0 \\ 0 & 0 & \varepsilon_3 \end{bmatrix} \tag{3}$$

When the PSR is subjected to an end-to-end tensile displacement $2u_0$, voltage can be generated between the top and the bottom electrodes under the open circuit condition, as illustrated by Fig. 1(*b*), or current can be generated under the short circuit condition, as illustrated by Fig. 1(*c*).

When the PSR is stretched, we are interested in how much voltage can be generated under a given applied strain e_{app}. We define *sensitivity* of the PSR as the partial derivative of the output voltage ϕ_0 under the open circuit condition with respect to the applied strain e_{app}

$$S = \frac{\partial\phi_0}{\partial e_{\text{app}}} \tag{4}$$

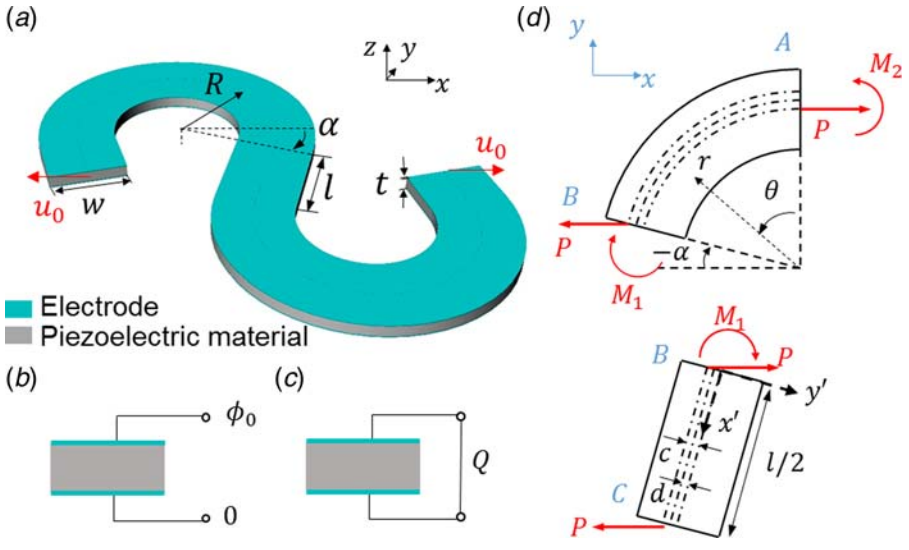

Fig. 1 (*a*) 3D schematic of a unit cell of a freestanding piezoelectric serpentine ribbon (PSR) with geometric parameters labels, (*b*) and (*c*) Cross-sectional view of the electrical boundary conditions (BCs) for open circuit (*b*) and short circuit (c), (*d*) Mechanical BCs for the arc and the arm; Weak BCs are adopted at the boundaries A, B, and C; c represents the offset of point loads and *d* represents the offset of the continuity point in the weak BC

The normalized sensitivity of the PSR is given by $\bar{S} = S/S_{\text{linear}}$, where S_{linear} is the sensitivity of its linear counterpart (see Appendix A):

$$S_{\text{linear}} = \frac{d_{31} Yt}{\varepsilon_3 (1 - Y d_{31}^2/\varepsilon_3)} \tag{5}$$

For a PSR with an arc angle α, when $\alpha \to -\pi/2$, the normalized sensitivity $\bar{S}$ must approach one because the serpentine ribbon degenerates to a linear one.

Next, we will apply linear elasticity and linear piezoelectricity theories to derive the normalized sensitivity $\bar{S}$ as a function of the normalized geometric parameters, l/R, w/R, and α. We establish the boundary value problem (BVP) by listing the equilibrium equation, compatibility equation, the constitutive law, and the boundary conditions (BCs) under the global Cartesian coordinate. The equilibrium equations are as follows:

$$\begin{aligned} \frac{\partial \sigma_{ij}}{\partial x_j} &= 0 \\ \frac{\partial D_i}{\partial x_i} &= 0 \end{aligned} \tag{6}$$

The compatibility equation is as follows:

$$\frac{\partial}{\partial x_j}\left(\frac{\partial e_{ij}}{\partial x_k} + \frac{\partial e_{jk}}{\partial x_i} - \frac{\partial e_{ik}}{\partial x_j}\right) = \frac{\partial^2 e_{jj}}{\partial x_i \partial x_k} \quad (i \neq j, j \neq k, \text{ no summation}) \tag{7}$$

The constitutive law is as follows:

$$\begin{aligned} e_{ij} &= c_{ijkl}\sigma_{kl} + d_{kij}E_k \\ D_k &= d_{kij}\sigma_{ij} + \varepsilon_{kj}E_j \end{aligned} \tag{8}$$

$\boldsymbol{e}$, $\boldsymbol{c}$, $\boldsymbol{\sigma}$, $\boldsymbol{E}$, and $\boldsymbol{D}$ denote the strain tensor, the compliance matrix, the stress tensor, the electric field, and the electric displacement, respectively. The solution procedure is outlined as follows: First, we prescribe an applied force P on the PSR, where P represents the reaction force when the PSR is stretched by e_{app} or when the unit cell is stretched by $2u_0$. According to the definition in Ref. [39], the mechanical stiffness of the PSR normalized by that of its linear counterpart can be expressed as $PL/(2Ywtu_0)$. Then we semi-analytically solve the output voltage ϕ_0 and the applied strain e_{app} as functions of P. Finally, the normalized sensitivity $\bar{S}$ can be obtained by canceling the applied force P. The normalized mechanical stiffness can also be analytically solved.

Similar to our previous model on nonbuckling serpentines using elasticity theory [39], due to the symmetry of the BCs, the unit cell can be reduced to a quarter cell subjected to a horizontal force P, which corresponds to a displacement of $u_0/2$. This quarter cell can be further disassembled into two subregions—a half arc and a half arm, as shown in Fig. 1(*d*). For the two subregions, the cylindrical coordinate $\{r, \theta, z\}$ is adopted for the arc, whereas a local Cartesian coordinate $\{x', y', z\}$ is used for the arm. Weak mechanical BCs such as point forces and moments are applied at the ends A, B, and C. An offset c for the point force P and an offset d for the continuity point are introduced as labeled in the figure to improve the accuracy of the results.

To solve the electromechanically coupled equation, the piezoelectric plate theory can be adopted because the piezoelectric serpentine is flat initially and deforms in-plane subsequently. Regarding the electrical BCs of the open circuit case (Fig. 1(*b*)), we assume the bottom surface ($z = 0$) is grounded and the top surface ($z = t$) has a constant electric potential ϕ_0, which needs to be determined as a function of P. All the sidewalls are insulated and charge-free. The electrical BCs can be written as follows:

$$\begin{cases} \phi = 0 & \text{on } z = 0 \\ \phi = \phi_0 & \text{on } z = t \\ D_i n_i = 0 & \text{on sidewalls} \end{cases} \tag{9}$$

where n_i represents the surface normal. Besides, the total free charge must be zero on each metallized surface for the open circuit condition:

$$Q_{\text{net}} = \int D_3 d\Omega = 0 \quad \text{on } z = 0, t \tag{10}$$

In this work, we assume the open circuit condition because calculating and measuring voltage output is easier for FEM and experiments, respectively. With the open circuit solution, the short circuit solution can be easily obtained by changing a few electrical BCs.

Due to the thinness of the PSR and zero applied load out-of-plane, the BVP falls into the plane-stress category. The out-of-plane stresses σ_{13}, σ_{23}, and σ_{33} are zero and the out-of-plane shear strains e_{13} and e_{23} can be neglected. According to the piezoelectric plate theory, the electric displacement component D_3 can be assumed to be independent of z [49]. Hence, the constitutive law given in Eq. (8) reduces to a plane problem

$$\begin{cases} e_{11} = c_{11}\sigma_{11} + c_{12}\sigma_{22} \underline{+ d_{31}E_3} \\ e_{22} = c_{21}\sigma_{11} + c_{22}\sigma_{22} \underline{+ d_{32}E_3} \\ e_{12} = c_{66}\sigma_{12} \\ e_{33} = c_{31}\sigma_{11} + c_{32}\sigma_{22} \underline{+ d_{33}E_3} \\ \underline{D_3 = d_{31}\sigma_{11} + d_{32}\sigma_{22} + \varepsilon_3 E_3} \end{cases} \tag{11}$$

For elastically isotropic material, the compliance matrix satisfies $c_{21} = c_{12} = c_{32} = c_{31} = -\nu/Y$, $c_{66} = (1+\nu)/Y$, and $c_{11} = c_{22} = 1/Y$. The indices 1, 2, and 3 represent the coordinates x, y, and z, respectively, in the global Cartesian coordinate. The underlined terms result from the piezoelectricity of the material. In other words, the underlined terms will disappear without piezoelectricity, and the problem will degenerate to the passive serpentine ribbon in our previous study [39]. The electrical fields can be further simplified [49] as follows:

$$\begin{cases} \phi = \phi^{(0)} + z\phi^{(1)} \\ E_i = 0,\ E_3 = E_3^{(0)} \\ D_i = 0,\ D_3 = D_3^{(0)} \end{cases} \tag{12}$$

where $i = 1, 2$. The terms $()^{(j)}$ are functions independent of z but may be dependent on x and y, where j represents the jth order term. Substituting Eq. (12) into the electrical BCs (Eq. (9)), the electric potential ϕ in the body is found to be independent of in-plane coordinates x and y but proportional to z, while the z component of the electric field, E_3, is a constant everywhere in the material. The z component of the electric displacement, D_3, which is independent of z but dependent on the in-plane coordinates x and y, can be obtained from Eq. (11). As a result, the electrical fields can be solved as follows:

$$\begin{cases} \phi = z\dfrac{\phi_0}{t} \\ E_i = 0,\ E_3 = -\dfrac{\phi_0}{t} \\ D_i = 0,\ D_3 = \varepsilon_3 E_3 + d_{31}\sigma_{11} + d_{32}\sigma_{22} \end{cases} \quad (i = 1, 2) \tag{13}$$

In terms of the mechanical fields, strain and stress fields were solved using the Airy stress function in our previous elasticity model for passive serpentine ribbons [39]. As for PSRs, the mechanical BCs and the equilibrium and compatibility equations should be identical to those of passive serpentine ribbons, while the only difference is the underlined terms in Eq. (11), which is the constitutive law. The strain components e_{ii} in Eq. (11) contain the underlined constant term $d_{3i}E_3$, which are subjected to the piezoelectric effect. The stress with undetermined offsets c for

passive serpentines must be the solution to the stress in the PSR, because the underlined terms do not cause any violation to any of the governing equations and BCs. A simple proof is shown in Appendix B.

Let $\hat{\boldsymbol{\sigma}}$ and $\hat{\boldsymbol{u}}$ represent the stress and displacement fields, respectively, in the global Cartesian coordinate for passive serpentines, with undetermined offsets c. For simplicity, we use $\hat{\boldsymbol{u}}^{\text{arc}}$ and $\hat{\boldsymbol{u}}^{\text{arm}}$ to distinguish displacements in the arm and the arc. With the stress field $\hat{\boldsymbol{\sigma}}$ available from passive serpentines, the in-plane strains in the global coordinate become

$$\begin{cases} e_{11} = \dfrac{1}{Y}(\hat{\sigma}_{11} - \nu\hat{\sigma}_{22}) \underline{+ d_{31}E_3} \\ e_{22} = \dfrac{1}{Y}(\hat{\sigma}_{22} - \nu\hat{\sigma}_{11}) \underline{+ d_{32}E_3} \\ \epsilon_{12} = \dfrac{\hat{\sigma}_{12}}{G} \end{cases} \tag{14}$$

where the underlined terms do not exist for passive serpentines since they do not have piezoelectric property. The electric displacement can be written as

$$D_3 = \varepsilon_3 E_3 + d_{31}\hat{\sigma}_{11} + d_{32}\hat{\sigma}_{22} \tag{15}$$

By substituting BC Eq. (10) and $E_3 = -\phi_0/t$ into Eq. (15), the relationship between the output voltage and the applied force can be obtained as

$$\phi_0 = \frac{t}{\varepsilon_3 A_s}\int (d_{31}\hat{\sigma}_{11} + d_{32}\hat{\sigma}_{22})d\Omega \tag{16}$$

where A_s is the in-plane area of the serpentine.

To further investigate the strain sensitivity of the PSR, we need to find out the relation between the applied strain and the reaction force. The displacement field in the global coordinate can be obtained from Eq. (14) by substituting $E_3 = -\phi_0/t$

$$\begin{cases} u_x^{\text{arc}} = \hat{u}_x^{\text{arc}} \underline{- d_{31}x\phi_0/t} \\ u_y^{\text{arc}} = \hat{u}_y^{\text{arc}} \underline{- d_{32}y\phi_0/t} \end{cases} \quad \begin{cases} u_x^{\text{arm}} = \hat{u}_x^{\text{arm}} \underline{- d_{31}x\phi_0/t} \\ u_y^{\text{arm}} = \hat{u}_y^{\text{arm}} \underline{- d_{32}y\phi_0/t} \end{cases} \tag{17}$$

where the underlined terms are attributed to the piezoelectricity of the ribbon. As we did for passive serpentines, an offset d of the continuity point between the arm and the arc is introduced to offset the inaccuracy due to the weak BCs. With d, the end-to-end displacement can be obtained as

$$u_{\text{app}} = \frac{u_0}{2} = u_x^{\text{arc}}|_{r=\frac{a+b}{2}+d,\ \theta=\frac{\pi}{2}+\alpha} + u_x^{\text{arm}}|_{x=\frac{l}{2},\ y=0} \tag{18}$$

Plugging Eq. (18) into Eq. (1), the relation between e_{app} and P can be obtained. Up to now, we can express both the output voltage ϕ_0 and the applied strain e_{app} in terms of the reaction force P. Calculating sensitivity according to Eq. (4), P can be fully eliminated. Thus, the normalized sensitivity of the PSR is a function of three independent normalized geometric parameters (w/R, l/R, α) and three independent normalized material parameters (ν, Yd_{31}^2/ε_3, d_{32}/d_{31}). Justification for the three independent normalized material parameters is offered in Appendix C.

However, two unknown offsets c and d still exist. As discussed for passive serpentines, given material, the offsets c and d must be functions of four in-plane geometric parameters (w, R, l, α). Thus, we define $c_0 = c(w, R, l \to 0, \alpha \to -\pi/2)$ and $d_0 = d(w, R, l \to 0, \alpha \to -\pi/2)$. The variations of c and d are proposed to be [39]

$$c = \begin{cases} c_0\left(\dfrac{2\alpha}{\pi}\right)^4 & \alpha \le 0 \\ 0 & \alpha > 0 \end{cases}, \quad d = \begin{cases} d_0\left(\dfrac{2\alpha}{\pi}\right)^4 & \alpha \le 0 \\ 0 & \alpha > 0 \end{cases} \tag{19}$$

c_0 and d_0 can be solved by setting the behavior of the PSR to be a linear piezoelectric ribbon when $l \to 0$ and $\alpha \to -\pi/2$. In our study, the sensitivity and effective stiffness degenerates to

$$\begin{aligned} &\frac{S_0}{S_{\text{linear}}} = 1 && \text{as } l \to 0,\ \alpha \to 0 \\ &\frac{PL}{2Ywtu_0} = \frac{1}{1 - Yd_{31}^2/\varepsilon_3} && \text{as } l \to 0,\ \alpha \to 0,\ \phi_0 \to \phi_{\text{linear}} \end{aligned} \tag{20}$$

By solving the two equations in Eq. (20) for the two unknowns c_0 and d_0 in MATHEMATICA, the normalized sensitivity can be finally obtained as a function of the in-plane geometric parameters $\bar{S}(w/R, l/R, \alpha)$ for a given material.

2.2 FEM. To validate our analytical solutions, we used commercial FEM software ABAQUS to perform 3D simulations on PSRs of different shapes. To be consistent with later experimental study, the piezoelectric material was chosen to be 28-μm-thick PVDF, which is elastically isotropic and electromechanically orthotropic. The two piezoelectric coefficients d_{31} and d_{32}, the dielectric constant ε_3, and the Young's modulus Y of the PVDF thin film have been measured in our previous study [38]. The other material properties can be found in material data sheet and literatures [50–52]. Hence, the following values were adopted in our FEM: Young's modulus $Y = 3.6$ GPa, Poisson's ratio $\nu = 0.34$, and

$$[d_{ij}] = \begin{bmatrix} 0 & 0 & 0 & 0 & -27 & 0 \\ 0 & 0 & 0 & -23 & 0 & 0 \\ 10 & 1 & -33 & 0 & 0 & 0 \end{bmatrix} \times 10^{-12}\ N/C$$
$$[\varepsilon_{ij}] = \begin{bmatrix} 61.09 & 0 & 0 \\ 0 & 76.144 & 0 \\ 0 & 0 & 90.54 \end{bmatrix} \times 10^{-12}\ F/m \tag{21}$$

Due to the symmetry of the serpentine, we analyzed half of the unit cell of the serpentine in FEM and applied periodic mechanical BCs, as shown in Fig. 2(*a*). The right end was fixed in the x-direction, but was free to move in the y-direction except for the bottom line of the right end. The left end was subjected to an applied strain e_{app} in the negative x-direction. To suppress the buckling, everywhere in the bottom surface was constrained in the z-direction. For the electrical BCs, the electric potential of the bottom surface ($z = 0$) was set to be 0, while that of the top surface ($z = t$) was an undetermined constant. Figure 2(*b*) shows the in-plane deformed configuration with a scale factor of 10 when $e_{\text{app}} = 1\%$. The output voltage, electric field, electric displacement, and mechanical deformation of the ribbons can be obtained as FEM results.

Figures 2(*c*)–2(*e*) display contour plots for the z component of the electric displacement (D_3) of three different serpentine shapes obtained by analytical methods (left panels) and FEM (right panels). It is obvious that the full-field analytical solution agrees well with the FEM solution except that some subtle mismatch occurs near the interface between the arm and the arc. It can be attributed to the fact that the weak BCs applied on the interface can cause some discontinuity in the stresses, displacements, and the electric displacements. Fortunately, extreme values occur at the crest of the arc, which is usually far enough from the interface unless $\alpha \to -\pi/2$. The contour plots in Fig. 2 indicate that the extreme values obtained by analytical and FEM solutions are very close. In Sec. 3, we will provide graphs to do more quantitative comparison.

2.3 Experiments. Tensile tests on freestanding PSRs were performed to validate the results of our analytical and FEM solutions. We purchased a pre-electroded and prepoled 28-μm-thick PVDF film (TE connectivity) to fabricate PSRs of different shapes using a paper/vinyl cutter plotter (Silhouette CAMEO). The material properties of this commercial PVDF were measured

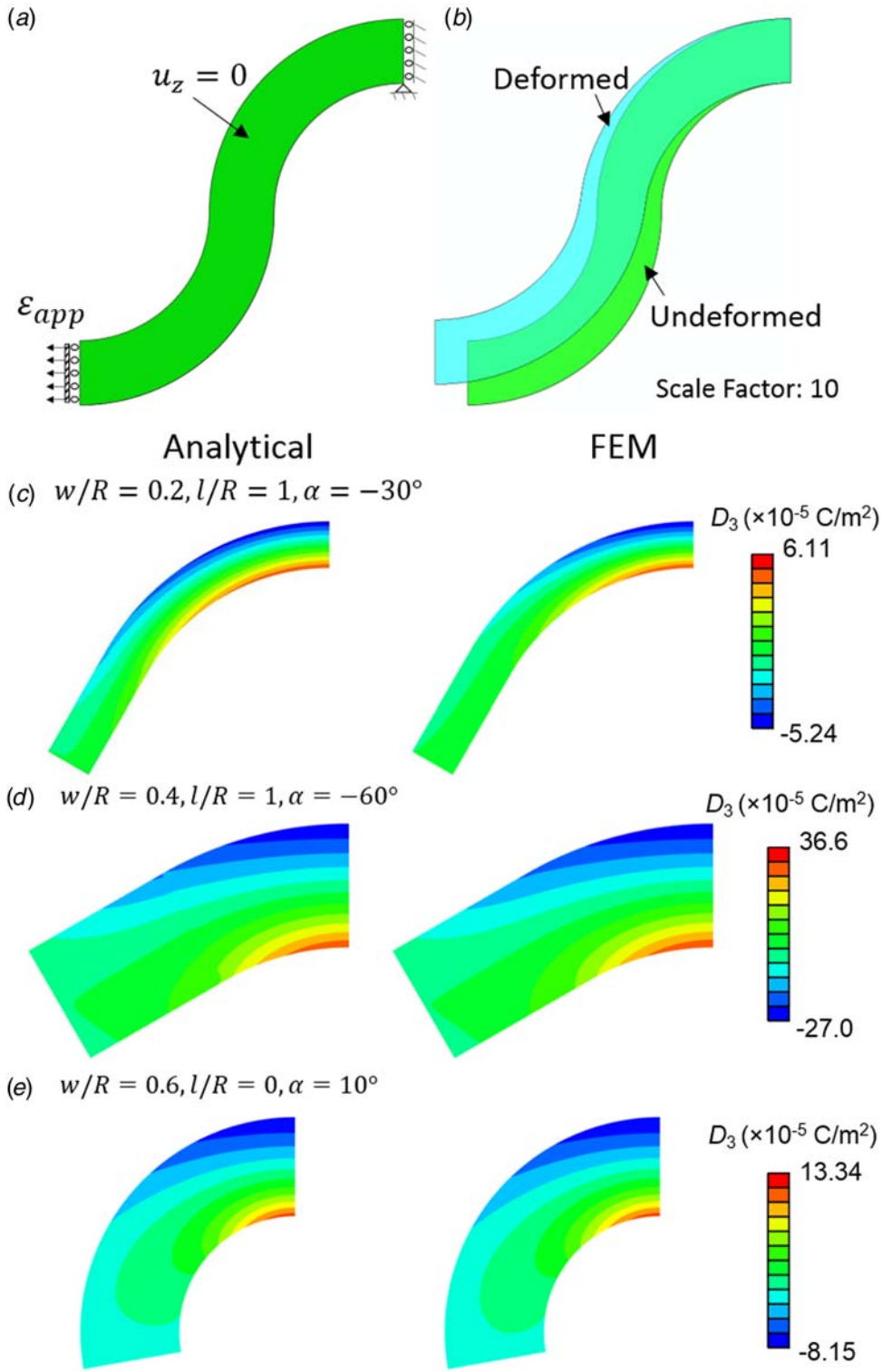

Fig. 2 (*a*) Mechanical boundary conditions in FEM, (*b*) 10× scaled deformed configuration obtained by FEM, and (c–e) Full-field contour plots for the *z*-component of the electric displacement D_3 solved by the analytical method (left panels) and the FEM (right panels) under 1% applied strain for different PSR shapes

by us in a previous study [38]. Since the freestanding PSRs started buckling under very small strains (e.g., 0.2%), we added two cover sheets to suppress the out-of-plane buckling of the PSR, as illustrated in Fig. 3(*a*). A 50-μm-thick spacer was applied between the two cover sheets. The two ends of the PSR were patterned into two rectangular regions for clamping and electrical connection.

The PSR was first prestrained to 0.5% and then subjected to a 1 Hz cyclic uniaxial strain with a peak-to-peak amplitude of e_{pp} = 0.4% via an RSA-G2 dynamic mechanical analyzer, as shown in Fig. 3(*b*). At such a low loading rate (0.256 mm/s), the loading process can be regarded as a quasi-static process. The output voltage between the two surface electrodes was measured by a

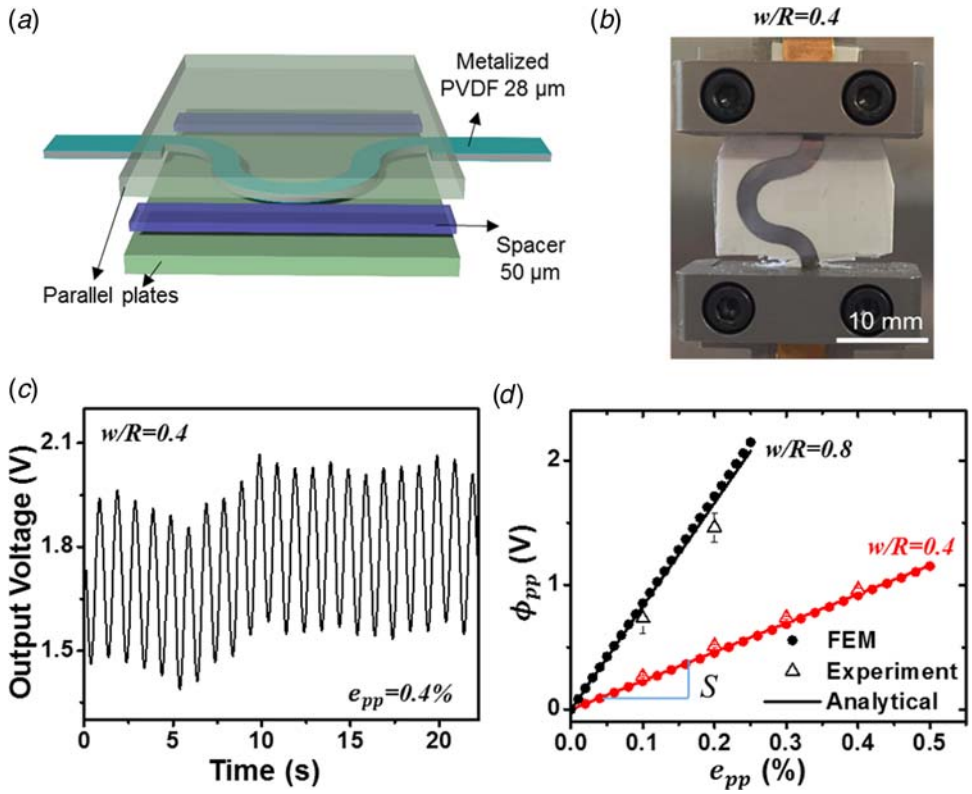

Fig. 3 (*a*) Experimental setup for limiting the out-of-plane buckling of PSRs under tension, (*b*) A PSR mounted on a dynamic mechanical analyzer, (c) As-measured output voltage of a PSR with $w/R = 0.4$, $l/R = 0$, $\alpha = 0$ deg, and $R = 4$ mm under 0.5% prestrain and 0.4% peak-to-peak strain amplitude, and (*d*) Peak-to-peak output voltage as a function of strain amplitude for the serpentine ribbons of $w/R = 0.8$ (black) and $w/R = 0.4$ (red) obtained by the analytical method (solid line), FEM (dots), and experiments (hollow triangles); Sensitivity is given by the slope of the linear curves

National Instrument data acquisition board (NI6225). Since the clamped regions did not generate voltage but did contribute to the total capacitance, the as-measured amplitude of the output voltage should be compensated. The compensation factor is given by $f = (A_c + A_a)/A_a$, where A_a is the area of the active region (the serpentine part shown in Figs. 3(*a*) and 3(*b*)) and A_c is the area of the clamped region (two rectangular terminal pads visible in Fig. 3(*a*)). Experimentally, we manufactured two PSRs with the same $\alpha = 0$, $l/R = 0$, and the same rectangular terminal pads but different $w/R = 0.4$ and 0.8. Their compensation factors were calculated to be $f_{0.4} = 2.04$ and $f_{0.8} = 1.66$. The as-measured output voltage for a PSR of $w/R = 0.4$, $\alpha = 0$, and $l/R = 0$ subjected to $e_{pp} = 0.4\%$ is plotted in Fig. 3(*c*). It is obvious that the output voltage cycles with the strain cycle at 1 Hz, so the peak-to-peak amplitude of the voltage oscillation (ϕ_{pp}) should be first compensated and then related to the amplitude of cyclic strain (e_{pp}). PSRs with different w/R and subjected to different e_{pp} were also measured. At least two specimens were measured for each shape. The compensated ϕ_{pp} versus e_{pp} results are plotted as hollow triangles with error bars in Fig. 3(*d*).

3 Results

3.1 Electromechanical Response. To compare with the experimental results, analytical and FEM results were obtained for the same shapes as the ones used in the experiments. They were stretched from the applied strains ($0.5\% - e_{pp}$) to ($0.5\% - e_{pp}$). The peak-to-peak voltage of each ribbon was obtained analytically and numerically as ϕ_{pp}. Analytical and FEM results are plotted as solid lines and solid dots in Fig. 3(*d*) for two different shapes—$w/R = 0.4$ and 0.8, both with $\alpha = 0$ and $l/R = 0$. Other serpentine shapes will be investigated in the following figures: according to Fig. 3(*d*), ϕ_{pp} is linearly proportional to e_{pp}, as expected for linear piezoelectric materials. The slope of the linear ϕ_{pp} versus e_{pp} curve is the sensitivity of the PSR defined by Eq. (4), which is dictated by the serpentine shape for a given material. According to Fig. 3(*d*), the larger w/R, the bigger the slope, which means more voltage can be generated using a wider ribbon. The six experimental results (hollow triangles) fall reasonably close to the other two solutions, which validates our analytical and FEM solutions.

3.2 The Sensitivity and Stiffness of PSRs. Within our linear theory, the sensitivity of PSRs is independent of e_{pp} and depends only on the serpentine shape. To reveal the effects of serpentine shapes, from now on, we will plot and discuss only the normalized sensitivity, $\bar{S}$. Figure 4 plots $\bar{S}$ as a function of the three different normalized geometric parameters. Solid curves represent the analytical solution, solid dots represent the FEM results, and the hollow triangles represent the experimental results. It is evident from Fig. 4 that all three types of solutions are in good agreement with each other. Slight discrepancies between the analytical and the FEM results occur at large w/R and small l/R in Figs. 4(*a*) and 4(*b*) as well as when $\alpha \to -\pi/2$ and l/R is large in Fig. 4(*c*) due to the weak BCs adopted, as we mentioned before. Overall, the dependences are all monotonic—large sensitivity can be achieved by using wide (large w/R), less wavy (small α), and short-armed (small l/R) PSRs. As $\bar{S}$ never exceeds 1, we conclude that linear ribbons set the upper limit of the sensitivity for the PSR, i.e., all PSRs are less sensitive than linear ribbons.

In comparison, Fig. 5 plots the effective mechanical stiffness of the PSRs using the same horizontal axes as Fig. 4. Due to the

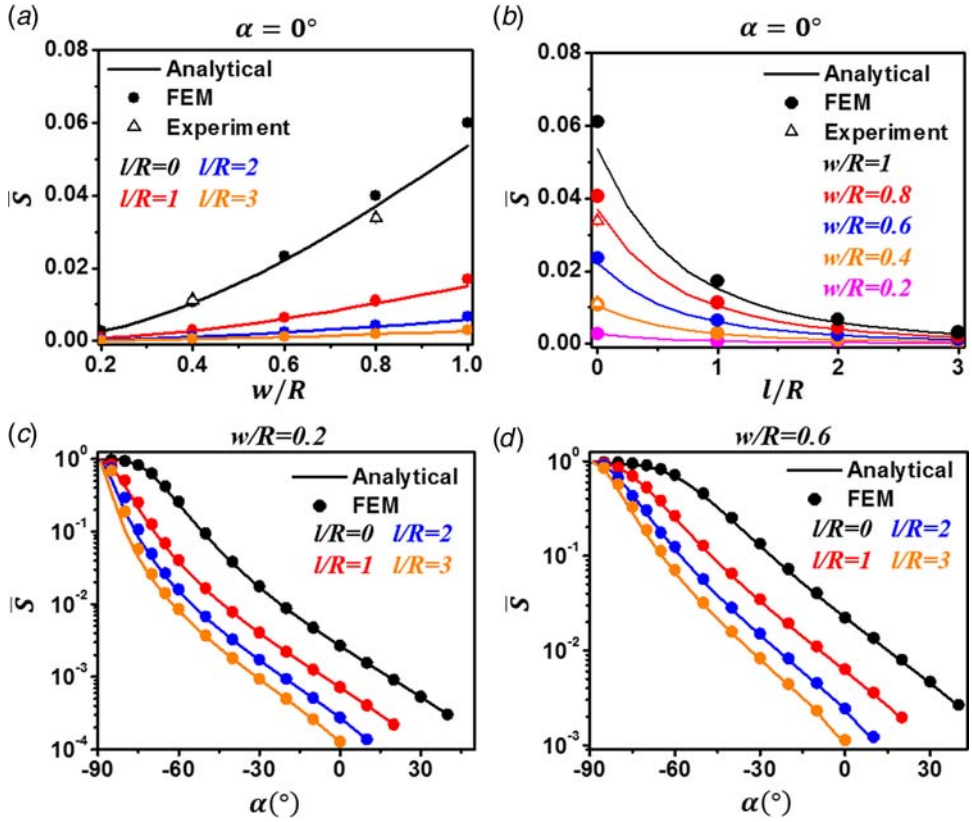

Fig. 4 Normalized sensitivity obtained by the analytical method (solid curve), FEM (dots), and experiments (hollow triangles): (*a*) and (*b*) $\alpha = 0$, (c) $w/R = 0.2$, and (*d*) $w/R = 0.6$

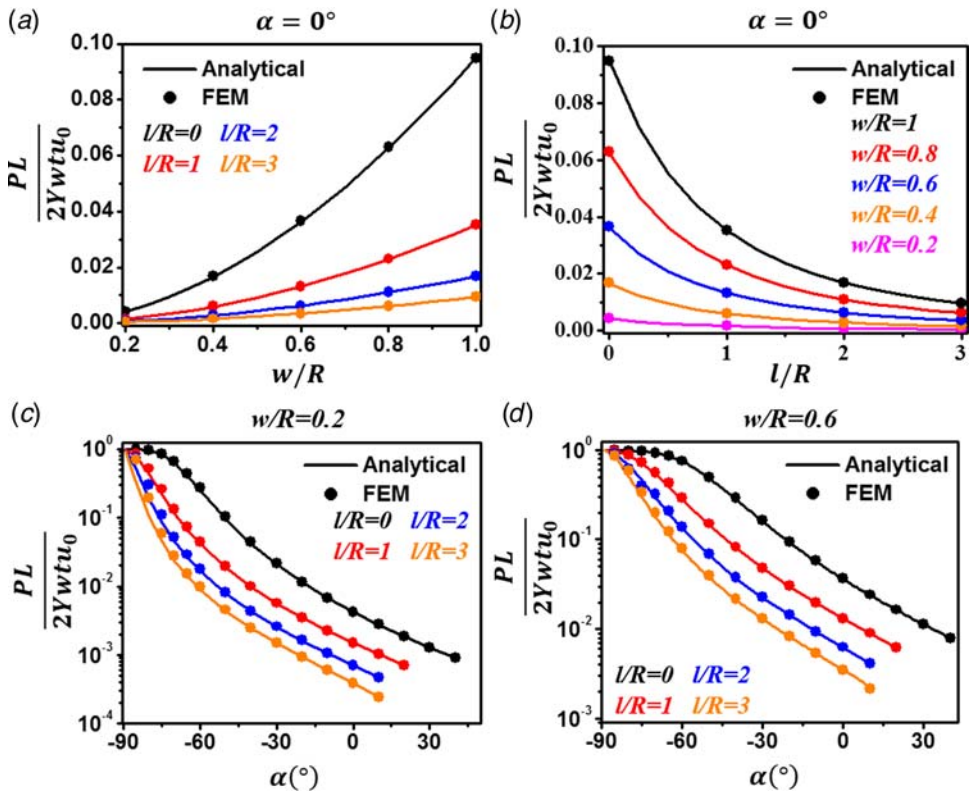

Fig. 5 Normalized stiffness obtained by the analytical method (solid curve) and FEM (dots): (*a*) and (*b*) $\alpha = 0$, (c) $w/R = 0.2$, and (*d*) $w/R = 0.6$

electromechanical coupling, the stiffness of the PSR and passive serpentine ribbons as offered in Ref. [39] differs slightly (~1%). Although the sensitivity and stiffness curves are not matched perfectly, they have a very similar trend, indicating that the softer serpentines are always less sensitive. This finding gives us a trade-off when designing soft and stretchable PSRs. We have to balance the needs for softness and sensitivity to decide on the PSR shape.

4 Discussion

4.1 Effects of the Weak BCs. Despite the decent agreement between the analytical and the FEM solutions, discrepancy exists including visible mismatch in Fig. 4(*c*) for nearly straight ($\alpha < -70$ deg) narrow ribbons ($w/R < 0.2$) with long arms ($l/R \geq 1$). Such imperfections of the analytical solution can be traced back to the application of the weak BCs in the full-field elasticity solution. As shown in Fig. 1(*d*), weak BCs, i.e., point loads instead of distributed loads, were applied at the free end of the arm C and at the arc–arm interface B. For a serpentine with large arc and arm, the error caused by the assumed point loads at C and B is negligible as the Saint-Venant's principle holds. Thus, our theoretical solution provides a reliable full-field solution to the stress and displacement. However, the Saint-Venant's principle breaks down for serpentines with small arcs. In this case, the weak BCs applied at B are so close to the crest of the serpentine that the "boundary layer" engulfs the whole arc.

In our elasticity models for passive serpentine ribbons [39], the offsets c and d as labeled in Fig. 1(*d*) were introduced in the BC to diminish the influences of the weak BCs on the maximum strain, but for the full-field solution, it works only for wide ribbons ($w/R > 0.6$). For narrow ribbons ($w/R < 0.2$) with a short arc ($\alpha < 70°$), it seems that such limitation cannot be fixed with the offsets.

4.2 PSRs Embedded in a Polymer Matrix. So far, we have presented the electromechanical response and the sensitivity of freestanding, nonbuckling PSRs. However, in many applications, the PSR is embedded in a polymer matrix, which can provide the necessary support and insulation. Figure 6(*a*) illustrates a PSR embedded in a polymer matrix of thickness t_m and Young's modulus Y_m. We expect that the sensitivity of the serpentine ribbons would increase due to the extra constraint from the polymer matrix, but no easy analytical solution is achievable at this point. We performed experiments on PSRs sandwiched by two Tegaderm tapes each with $t_m =$ 47 μm, $Y_m = 7.4$ MPa [35], and $\nu = 0.49$. We used a 28-μm-thick PVDF to fabricate the PSR, $t_{PVDF} = 28$ μm and $Y_{PVDF} = 3.6$ GPa. For such matrix-embedded PSRs, the sensitivity is a function of not only the geometry of the PSR but also the thickness ratio and the modulus ratio of the matrix and the serpentine, i.e., $\bar{S}(w/R,\ l/R,\ \alpha,\ t_m/t_{PVDF},\ Y_m/Y_{PVDF})$. We patterned the PVDF into PSRs of $l/R = 0$ and $\alpha = 0°$ but different w/R (0.4, 0.6, and 0.8) and then sandwiched them by Tegaderm with the terminal pads exposed for electrical connection. The sandwiched specimens were subjected to a prestretch of 0.3% and a cyclic test with $e_{pp} =$ 0.2% at a frequency of 1 Hz. The cyclic tests were repeated three times for each specimen. Representative as-measured output voltages of the three different types of PSRs are displayed in Fig. 6(*b*). Experimentally measured sensitivity was obtained following the same peak-to-peak voltage compensation and slope extraction procedure as described for freestanding PSRs in Sec. 2.3. The experimentally measured sensitivity was normalized and plotted as hollow triangles in Fig. 6(*c*).

We also performed FEM for embedded PSRs to reveal the effects of the thickness and Young's modulus of the polymer matrix on the sensitivity of the matrix-embedded PSRs. Figure 6(*c*) plots the FEM results of $\bar{S}$ versus t_m in solid dots, with the given Young's moduli $Y_{PVDF} = 3.6$ GPa and $Y_m = 7.4$ MPa. As expected,

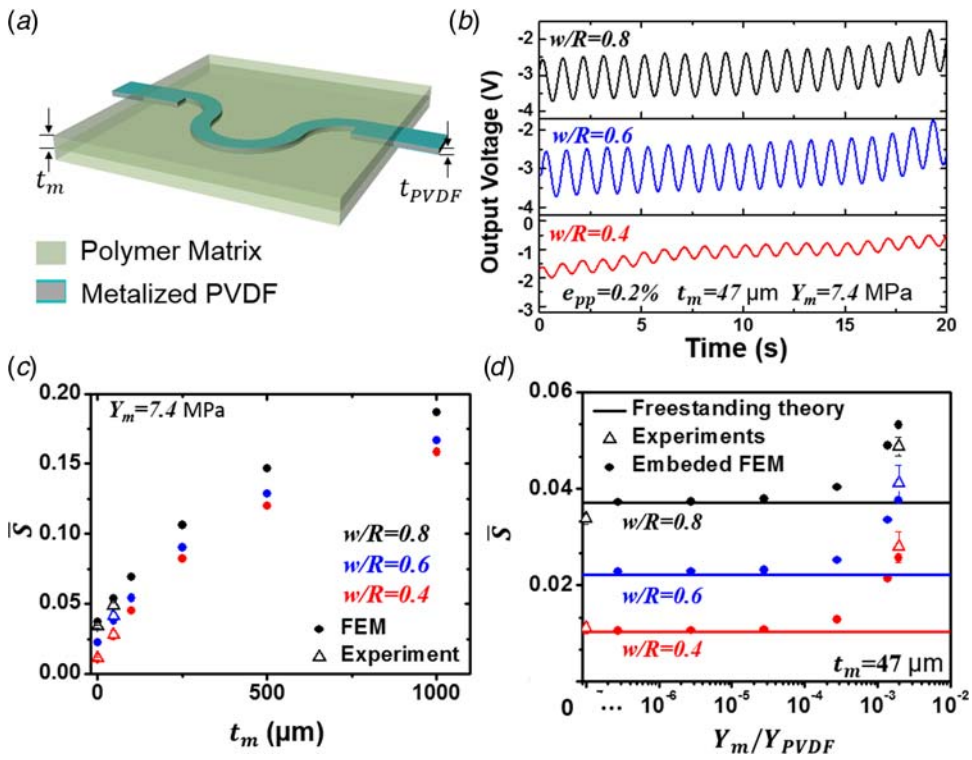

Fig. 6 (*a*) A schematic of matrix-embedded PSR, (*b*) As-measured output voltage for Tegaderm-sandwiched PVDF PSRs of different widths under a prestrain of 0.3% and a peak-to-peak strain amplitude of 0.2%, (*c*) Normalized sensitivity as a function of matrix thickness obtained by FEM (dot) and experiments (hollow triangle), and (*d*) $\bar{S}$ as a function of the modulus ratio Y_m/Y_{PVDF}; Solid lines are analytical solutions to freestanding PSRs, while the dots and hollow triangles are FEM and experimental results, respectively, of matrix-embedded serpentines

$\bar{S}$ increases monotonically with t_m till it eventually saturates when the polymer matrix can be considered as infinitely thick. The experimental results of the Tegaderm-sandwiched PSRs agreed well with the FEM results in Fig. 6(*c*).

Effects of matrix stiffness are investigated in Fig. 6(*d*). Assuming matrix thickness $t_m = 47$ μm is fixed but matrix modulus is changing, Fig. 6(*d*) plots the FEM and experimental results of $\bar{S}$ versus Y_m/Y_{PVDF} (log-scale) for three different w/R (0.4, 0.6, and 0.8). Two useful observations can be made. First, experimental results are in good agreement with the FEM results. Second, $\bar{S}$ increases monotonically with Y_m/Y_{PVDF} but when Y_m/Y_{PVDF} approaches zero, i.e., the infinitely soft substrate, $\bar{S}$ approaches a constant that must be the same as the $\bar{S}$ of freestanding PSRs. For comparison, we also plot the analytically solved $\bar{S}$ of freestanding PSRs as horizontal solid lines. We can see that when $Y_m/Y_{\text{PVDF}} < 3 \times 10^{-5}$, the FEM solution to embedded PSRs and the analytical solution to freestanding PSRs are indistinguishable.

5 Conclusion

We have developed a full-field analytical solution to freestanding, nonbuckling PSRs under small deformation by combining the elasticity solution to passive serpentines with the piezoelectric plate theory. We also performed FEM and carried out experiments to validate our analytical solution. We emphasized that the experimentally measured peak-to-peak output voltage should be properly compensated because the clamped terminal pads do not contribute to the output voltage but do contribute to the total capacitance. After proper compensation, all three types of results show excellent agreement and confirm that the peak-to-peak output voltage is linearly proportional to the peak-to-peak applied strain. The effects of serpentine geometry on PSR sensitivity were fully studied. The sensitivity of the PSR has very similar geometric dependence as the stiffness of PSR, which indicates a direct trade-off between the sensitivity and the softness. Overall, the sensitivity is always lower than its linear counterpart but improves with increasing w/R and decreasing l/R and α. We have also studied the effect of the polymer matrix on the sensitivity of PSRs and found that the increasing matrix thickness and Young's modulus can improve the sensitivity of the PSR. We also proved that our analytical solution is applicable to serpentines made out of stiffness materials but embedded in a very soft matrix.

Acknowledgment

This work is supported by the Young Investigator Program (YIP) of Air Force Office of Scientific Research (AFOSR) under Grant No. FA9550-15-1-0112 and the NSF CMMI Grant No. 1351875. S.L. acknowledges the Warren A. and Alice L. Meyer Endowed Scholarship in Engineering at the University of Texas at Austin.

Appendix A

For a straight piezoelectric ribbon under uniaxial stretching, the governing Eqs. (6)–(8) and the BCs Eqs. (9) and (10) still hold. The only nonzero stress is the normal stress σ_{11} in the stretching direction, so the constitutive law gives

$$\begin{aligned} \varepsilon_{11} &= \frac{\sigma_{11}}{Y} + d_{31}E_3 \\ D_3 &= d_{31}\sigma_{11} + \varepsilon_3 E_3 \end{aligned} \tag{A1}$$

σ_{11} is constant over the ribbon. Since $\phi = -E_3 t$, the BC Eq. (9) gives

$$\phi_{\text{linear}} = \frac{d_{31}Yt}{\varepsilon_3(1 - Yd_{31}^2/\varepsilon_3)} e_{11} \tag{A2}$$

The applied strain $e_{\text{app}} = e_{11}$, so the sensitivity of a straight piezoelectric ribbon is

$$S_{\text{linear}} = \frac{\partial \phi_{\text{linear}}}{\partial e_{\text{app}}} = \frac{d_{31}Yt}{\varepsilon_3(1 - Yd_{31}^2/\varepsilon_3)} \tag{A3}$$

Appendix B

To prove the stress field $\hat{\boldsymbol{\sigma}}$ for passive serpentine is the solution for the PSR, we need to prove $\hat{\boldsymbol{\sigma}}$ satisfies all the governing Eqs. (6)–(8) and all the mechanical BCs. Keep in mind that $\hat{\boldsymbol{\sigma}}$ in the arc and the arm was derived in the local cylindrical coordinate, $\{r, \theta\}$, and the local Cartesian coordinate, $\{x', y'\}$, respectively, as shown in Fig. 1(*d*). To apply the constitutive law, we must transform the local coordinates $\{r, \theta\}$ and $\{x', y'\}$ to the global coordinate $\{x, y\}$ with transformation angles $\phi_1 = -(\pi/2 + \theta)$ and $\phi_2 = -(\pi/2 + \alpha)$. Such rotation of axes does not affect the satisfaction of all the governing equations. Since the mechanical BCs and equilibrium equations of PSRs are identical to those of the passive serpentines, $\hat{\boldsymbol{\sigma}}$ automatically satisfies all the mechanical BCs and equilibrium equations of PSRs. Then, we need to prove that it satisfies the compatibility equation. The BVP can be reduced to a plane problem for PSRs, so the constitutive law gives Eq. (14). For a plane problem, the compatibility equation is

$$\frac{\partial^2 e_{11}}{\partial y^2} + \frac{\partial^2 e_{22}}{\partial x^2} = 2\frac{\partial^2 e_{12}}{\partial x \partial y} \tag{B1}$$

According to Eq. (13), the underlined terms in Eq. (14) are constant because E_3 is constant in the material. The compatibility Eq. (B1) is then satisfied even with the underlined terms because they do not contribute to the partial derivatives of the strains. Therefore, the stress field $\hat{\boldsymbol{\sigma}}$ with the undetermined c is the solution for our problem. The unknown c will be determined at last.

Appendix C

There are only five independent material properties, ν, Y, d_{31}, d_{32}, and ε_3, contributing to the voltage output of nonbuckling freestanding PSRs under uniaxial stretching. These five material properties can be further reduced to three independent normalized material properties. According to the analytical solution for passive serpentines [39], stress is proportional to the applied force

$$\hat{\sigma}_{ij} = \frac{P}{tR} f\left(\frac{r}{R}, \frac{w}{R}, \frac{l}{R}, \nu, \alpha\right) \tag{C1}$$

According to Eq. (16), the voltage is

$$\phi_0 = \frac{d_{31}}{\varepsilon_3}\frac{P}{R} g\left(\frac{w}{R}, \frac{l}{R}, \nu, \alpha, \frac{d_{32}}{d_{31}}\right) \tag{C2}$$

where f and g are dimensionless functions. Equations (1), (17), and (18) give the applied strain

$$\begin{aligned} e_{\text{app}} = {} & \frac{P}{YtR} f(w/R, l/R, \alpha, \nu) \\ & + \frac{d_{31}^2 P}{\varepsilon_3 tR} g(w/R, l/R, \alpha, \nu, d_{32}/d_{31}) \end{aligned} \tag{C3}$$

Then the sensitivity is

$$S = \frac{\partial \phi_0}{\partial e_{\text{app}}} = \frac{d_{31}PtY}{\varepsilon_3} \frac{g}{f + \frac{d_{31}^2 Y}{\varepsilon_3} g} \tag{C4}$$

By normalization, the factor $d_{31}PhY/\varepsilon_3$ can be canceled

$$\bar{S} = \frac{g}{g_{\text{linear}}} \frac{f_{\text{linear}} + \dfrac{d_{31}^2 Y}{\varepsilon_3} g_{\text{linear}}}{f + \dfrac{d_{31}^2 Y}{\varepsilon_3} g} \tag{C5}$$

Therefore, $\bar{S}$ is determined only by three normalized material properties ν, d_{32}/d_{31}, and $d_{31}^2 Y/\varepsilon_3$.

References

[1] Kim, D.-H., Ghaffari, R., Lu, N., and Rogers, J. A., 2012, "Flexible and Stretchable Electronics for Biointegrated Devices," Annu. Rev. Biomed. Eng., **14**, pp. 113–128.

[2] Someya, T., Bao, Z., and Malliaras, G. G., 2016, "The Rise of Plastic Bioelectronics," Nature, **540**(7633), pp. 379–385.

[3] Choi, C., Choi, M. K., Liu, S., Kim, M. S., Park, O. K., Im, C., Kim, J., Qin, X., Lee, G. J., and Cho, K. W., 2017, "Human Eye-Inspired Soft Optoelectronic Device Using High-Density MoS 2-Graphene Curved Image Sensor Array," Nat. Commun., **8**(1), pp. 1664.

[4] Ko, H. C., Stoykovich, M. P., Song, J., Malyarchuk, V., Choi, W. M., Yu, C.-J., Geddes Iii, J. B., Xiao, J., Wang, S., and Huang, Y., 2008, "A Hemispherical Electronic Eye Camera Based on Compressible Silicon Optoelectronics," Nature, **454**(7205), pp. 748–753.

[5] Hammock, M. L., Chortos, A., Tee, B. C. K., Tok, J. B. H., and Bao, Z., 2013, "25th Anniversary Article: The Evolution of Electronic Skin (E-Skin): A Brief History, Design Considerations, and Recent Progress," Adv. Mater., **25**(42), pp. 5997–6038.

[6] Dai, Z., Wang, Y., Liu, L., Liu, X., Tan, P., Xu, Z., Kuang, J., Liu, Q., Lou, J., and Zhang, Z., 2016, "Hierarchical Graphene-Based Films With Dynamic Self-Stiffening for Biomimetic Artificial Muscle," Adv. Funct. Mater., **26**(38), pp. 7003–7010.

[7] Lanzara, G., Salowitz, N., Guo, Z., and Chang, F. K., 2010, "A Spider-Web-Like Highly Expandable Sensor Network for Multifunctional Materials," Adv. Mater., **22**(41), pp. 4643–4648.

[8] Kaltenbrunner, M., White, M. S., Głowacki, E. D., Sekitani, T., Someya, T., Sariciftci, N. S., and Bauer, S., 2012, "Ultrathin and Lightweight Organic Solar Cells With High Flexibility," Nat. Commun., **3**, pp. 770.

[9] Jang, K.-I., Li, K., Chung, H. U., Xu, S., Jung, H. N., Yang, Y., Kwak, J. W., Jung, H. H., Song, J., and Yang, C., 2017, "Self-Assembled Three Dimensional Network Designs for Soft Electronics," Nat. Commun., **8**, 15894.

[10] Jaffe, H., and Berlincourt, D., 1965, "Piezoelectric Transducer Materials," Proc. IEEE, **53**(10), pp. 1372–1386.

[11] Bateman, T., 1962, "Elastic Moduli of Single-Crystal Zinc Oxide," J. Appl. Phys., **33**(11), pp. 3309–3312.

[12] Vinogradov, A., and Holloway, F., 1999, "Electro-Mechanical Properties of the Piezoelectric Polymer PVDF," Ferroelectrics, **226**(1), pp. 169–181.

[13] Kim, D.-H., Song, J., Choi, W. M., Kim, H.-S., Kim, R.-H., Liu, Z., Huang, Y. Y., Hwang, K.-C., Zhang, Y.-w., and Rogers, J. A., 2008, "Materials and Noncoplanar Mesh Designs for Integrated Circuits with Linear Elastic Responses to Extreme Mechanical Deformations," Proc. Natl. Acad. Sci., **105**, pp. 18675–18680.

[14] Kim, D. H., Xiao, J., Song, J., Huang, Y., and Rogers, J. A., 2010, "Stretchable, Curvilinear Electronics Based on Inorganic Materials," Adv. Mater., **22**(19), pp. 2108–2124.

[15] Kim, D.-H., Lu, N., Ghaffari, R., Kim, Y.-S., Lee, S. P., Xu, L., Wu, J., Kim, R.-H., Song, J., and Liu, Z., 2011, "Materials for Multifunctional Balloon Catheters With Capabilities in Cardiac Electrophysiological Mapping and Ablation Therapy," Nat. Mater., **10**(4), pp. 316–323.

[16] Xu, S., Zhang, Y., Cho, J., Lee, J., Huang, X., Jia, L., Fan, J. A., Su, Y., Su, J., and Zhang, H., 2013, "Stretchable Batteries With Self-Similar Serpentine Interconnects and Integrated Wireless Recharging Systems," Nat. Commun., **4**, pp. 1543.

[17] Song, J., 2015, "Mechanics of Stretchable Electronics," Curr. Opin. Solid State Mater. Sci., **19**(3), pp. 160–170.

[18] Rogers, J. A., 2015, "Conformal Piezoelectric Systems for Clinical and Experimental Characterization of Soft Tissue Biomechanics," Nat. Mater. **14**, 728–736.

[19] Dong, W., Xiao, L., Hu, W., Zhu, C., Huang, Y., and Yin, Z., 2017, "Wearable Human–Machine Interface Based on PVDF Piezoelectric Sensor," Trans. Inst. Meas. Control, **39**(4), pp. 398–403.

[20] Qi, Y., Kim, J., Nguyen, T. D., Lisko, B., Purohit, P. K., and McAlpine, M. C., 2011, "Enhanced Piezoelectricity and Stretchability in Energy Harvesting Devices Fabricated From Buckled PZT Ribbons," Nano Lett., **11**(3), pp. 1331–1336.

[21] Ma, T., Wang, Y., Tang, R., Yu, H., and Jiang, H., 2013, "Pre-Patterned ZnO Nanoribbons on Soft Substrates for Stretchable Energy Harvesting Applications," J. Appl. Phys., **113**(20), 204503.

[22] Li, Y., Fang, B., Zhang, J., and Song, J., 2011, "Surface Effects on the Wrinkling of Piezoelectric Films on Compliant Substrates," J. Appl. Phys., **110**(11), 114303.

[23] Song, S., and Yun, K.-S., 2015, "Design and Characterization of Scalable Woven Piezoelectric Energy Harvester for Wearable Applications," Smart Mater. Struct., **24**(4), 045008.

[24] Yun, D., and Yun, K.-S., 2013, "Woven Piezoelectric Structure for Stretchable Energy Harvester," Electron. Lett., **49**(1), pp. 65–66.

[25] Yun, D., Park, J., and Yun, K.-S., 2015, "Highly Stretchable Energy Harvester Using Piezoelectric Helical Structure for Wearable Applications," Electron. Lett., **51**(3), pp. 284–285.

[26] Gray, D. S., Tien, J., and Chen, C. S., 2004, "High-Conductivity Elastomeric Electronics," Adv. Mater., **16**(5), pp. 393–397.

[27] Li, T., Suo, Z. G., Lacour, S. P., and Wagner, S., 2005, "Compliant Thin Film Patterns of Stiff Materials as Platforms for Stretchable Electronics," J. Mater. Res., **20**(12), pp. 3274–3277.

[28] Hsu, Y. Y., Gonzalez, M., Bossuyt, F., Axisa, F., Vanfleteren, J., and De Wolf, I., 2009, "In Situ Observations on Deformation Behavior and Stretching-Induced Failure of Fine Pitch Stretchable Interconnect," J. Mater. Res., **24**(12), pp. 3573–3582.

[29] Jong-Hyun, A., and Jung Ho, J., 2012, "Stretchable Electronics: Materials, Architectures and Integrations," J. Phys. D Appl. Phys., **45**(10), 103001.

[30] Zhang, Y., Fu, H., Su, Y., Xu, S., Cheng, H., Fan, J. A., Hwang, K.-C., Rogers, J. A., and Huang, Y., 2013, "Mechanics of Ultra-Stretchable Self-Similar Serpentine Interconnects," Acta Mater., **61**(20), pp. 7816–7827.

[31] Widlund, T., Yang, S., Hsu, Y.-Y., and Lu, N., 2014, "Stretchability and Compliance of Freestanding Serpentine-Shaped Ribbons," Int. J. Solids Struct., **51**(23), pp. 4026–4037.

[32] Shyu, T. C., Damasceno, P. F., Dodd, P. M., Lamoureux, A., Xu, L. Z., Shlian, M., Shtein, M., Glotzer, S. C., and Kotov, N. A., 2015, "A Kirigami Approach to Engineering Elasticity in Nanocomposites Through Patterned Defects," Nat. Mater., **14**(8), pp. 785–789.

[33] Yang, S., Choi, I. S., and Kamien, R. D., 2016, "Design of Super-Conformable, Foldable Materials via Fractal Cuts and Lattice Kirigami," MRS Bull., **41**(2), pp. 130–137.

[34] Tang, Y. C., and Yin, J., 2017, "Design of Cut Unit Geometry in Hierarchical Kirigami-Based Auxetic Metamaterials for High Stretchability and Compressibility," Extreme Mech. Lett., **12**, pp. 77–85.

[35] Yang, S., Chen, Y. C., Nicolini, L., Pasupathy, P., Sacks, J., Becky, S., Yang, R., Daniel, S., Chang, Y. F., Wang, P., Schnyer, D., Neikirk, D., and Lu, N., 2015, "'Cut-and-Paste' Manufacture of Multiparametric Epidermal Sensor Systems," Adv. Mater., **27**(41), pp. 6423–6430.

[36] Huang, Y., Ding, Y., Bian, J., Su, Y., Zhou, J., Duan, Y., and Yin, Z., 2017, "Hyper-Stretchable Self-Powered Sensors Based on Electrohydrodynamically Printed, Self-Similar Piezoelectric Nano/Microfibers, Nano Energy, **40**, pp. 432–439.

[37] Duan, Y., Ding, Y., Bian, J., Xu, Z., Yin, Z., and Huang, Y., 2017, "Ultra-Stretchable Piezoelectric Nanogenerators via Large-Scale Aligned Fractal Inspired Micro/Nanofibers," Polymers, **9**(12), 714.

[38] Ha, T., Tran, J., Liu, S., Jang, H., Mitbander, R., Huh, H., Qiu, Y., Duong, J., Wang, R., Wang, P., Tandon, A., Sirohi, J., and Lu, N., 2019, "A Chest-Laminated Ultrathin and Stretchable E-Tattoo for the Measurement of Electrocardiogram, Seismocardiogram, and Cardiac Time Intervals," In submission.

[39] Yang, S., Qiao, S., and Lu, N., 2017, "Elasticity Solutions to Nonbuckling Serpentine Ribbons," J. Appl. Mech., **84**(2), pp. 021004.

[40] Fan, Z., Zhang, Y., Ma, Q., Zhang, F., Fu, H., Hwang, K.-C., and Huang, Y., 2016, "A Finite Deformation Model of Planar Serpentine Interconnects for Stretchable Electronics," Int. J. Solids Struct., **91**, pp. 46–54.

[41] Fan, Z., Wu, J., Ma, Q., Liu, Y., Su, Y., and Hwang, K.-C., 2017, "Post-Buckling Analysis of Curved Beams," J. Appl. Mech., **84**(3), 031007.

[42] Liu, L., and Lu, N., 2016, "Variational Formulations, Instabilities and Critical Loadings of Space Curved Beams," Int. J. Solids Struct., **87**, pp. 48–60.

[43] Zhang, Y., Xu, S., Fu, H., Lee, J., Su, J., Hwang, K.-C., Rogers, J. A., and Huang, Y., 2013, "Buckling in Serpentine Microstructures and Applications in Elastomer-Supported Ultra-Stretchable Electronics With High Areal Coverage," Soft Matter, **9**(33), pp. 8062–8070.

[44] Hsu, Y.-Y., Papakyrikos, C., Liu, D., Wang, X., Raj, M., Zhang, B., and Ghaffari, R., 2014, "Design for Reliability of Multi-Layer Stretchable Interconnects," J. Micromech. Microeng., **24**(9), 095014.

[45] Su, Y., Ping, X., Yu, K. J., Lee, J. W., Fan, J. A., Wang, B., Li, M., Li, R., Harburg, D. V., and Huang, Y., 2017, "In-Plane Deformation Mechanics for Highly Stretchable Electronics," Adv. Mater., **29**(8), 1604989.

[46] Pan, T., Pharr, M., Ma, Y., Ning, R., Yan, Z., Xu, R., Feng, X., Huang, Y., and Rogers, J. A., 2017, "Experimental and Theoretical Studies of Serpentine Interconnects on Ultrathin Elastomers for Stretchable Electronics," Adv. Funct. Mater. **27**(37), pp. 1702589.

[47] Bian, J., Ding, Y., Duan, Y., Wan, X., and Huang, Y., 2017, "Buckling-Driven Self-Assembly of Self-Similar Inspired Micro/Nanofibers for Ultra-Stretchable Electronics," Soft Matter, **13**, pp. 7244–7254.

[48] Dong, W., Zhu, C., Ye, D., and Huang, Y., 2017, "Optimal Design of Self-Similar Serpentine Interconnects Embedded in Stretchable Electronics," Appl. Phys. A, **123**(6), pp. 428.

[49] Rogacheva, N. N., 1994, *The Theory of Piezoelectric Shells and Plates*, CRC Press, Boca Raton, Florida.

[50] Varadan, V., Roh, Y., Varadan, V., and Tancrell, R., 1989, "Measurement of all the Elastic and Dielectric Constants of Poled PVDF Films," Proceedings of the IEEE 1989 Ultrasonics Symposium, IEEE, pp. 727–730.

[51] Seminara, L., Capurro, M., Cirillo, P., Cannata, G., and Valle, M., 2011, "Electromechanical Characterization of Piezoelectric PVDF Polymer Films for Tactile Sensors in Robotics Applications," Sens. Actuators A Phys., **169**(1), pp. 49–58.

[52] Nix, E., and Ward, I., 1986, "The Measurement of the Shear Piezoelectric Coefficients of Polyvinylidene Fluoride," Ferroelectrics, **67**(1), pp. 137–141.